Kyle Lourenssen
School of Engineering,
University of Guelph,
Guelph, ON, N1G 2W1, Canada
e-mail: kyle.lourenssen@gmail.com

James Williams
School of Engineering,
University of Guelph,
Guelph, ON, N1G 2W1, Canada
e-mail: jwilli29@uoguelph.ca

Faraz Ahmadpour
School of Engineering,
University of Guelph,
Guelph, ON, N1G 2W1, Canada
e-mail: fahmadpo@uoguelph.ca

Ryan Clemmer
School of Engineering,
University of Guelph,
Guelph, ON, N1G 2W1, Canada
e-mail: rclemmer@uoguelph.ca

S. Andrew Gadsden
School of Engineering,
University of Guelph,
Guelph, ON, N1G 2W1, Canada
e-mail: gadsden@uoguelph.ca

Syeda Humaira Tasnim[1]
School of Engineering,
University of Guelph,
Guelph, ON, N1G 2W1, Canada
e-mail: stasnim@uoguelph.ca

Design, Development, and Testing of a Low-Concentration Vanadium Redox Flow Battery

The purpose of this paper is to highlight the design, development, and testing of a low-concentration vanadium redox flow battery (VRFB). The low-cost implementation has a 7 cm × 7 cm active membrane area and an electrolyte volume of 450 mL for each positive and negative electrolyte. The electrolyte concentration is approximately 0.066 M vanadium. An H-cell for performing electrolysis with the electrolytes is developed, and the process and method for creating the electrolyte for this low-concentration implementation are described and documented. The maximum power density and energy efficiency of the battery among tests between 500 and 800 mA are 1.32 W/L and 28.51%, respectively. Results are presented in terms of polarization curves, charge/discharge cycles, and voltage, coulombic, and energy efficiencies. Adaptation of a COMSOL Multiphysics model is implemented to compare the computational performance figures and the results of our VRFB implementation. The numerical results agree with experimentation, and differences in the results can be attributed to the losses present in the experimental tests. The proposed battery and design are intended to investigate the performance and feasibility of a low-concentration VRFB. The ultimate long-term objective of this research is the development of a novel, cost-effective, and safe redox flow battery using hydrogen peroxide as one of the electrolytes.
[DOI: 10.1115/1.4046869]

Keywords: analysis and design of components, devices, and systems, batteries, flow batteries

1 Introduction

As the demand for sustainable and renewable energy sources grows, the need for cost-effective and reliable energy storage locations becomes increasingly important. Renewable energy power sources seldomly generate the consistent power required by the grid [1]. Through conversion and storage of renewable energy power, the energy can be properly deployed in a controlled fashion and intermitted production concerns can be minimized [1].

Various energy storage techniques are used by utility providers and industry, all with diverse advantages and disadvantages. Recently, the nature-derived sodium-ion battery was studied by Miroshnikov et al. [2], and characterizations of water in the salt electrolyte for electrochemical double-layer capacitors are performed by Mahankali et al. [3]. The redox flow battery (RFB) is an emerging energy storage device suited for large-scale applications. RFBs employ a reversible redox reaction to facilitate the storage of energy. The novel characteristic of this style of battery is the independence of the systems' energy capacity and energy potential. In some applications, these batteries can fully charge and discharge without substantial negative effects on the cell's components, giving this technology an advantage over many other storage techniques [4]. RFBs are a competitive prospect for future pairing with renewable energy production and a more sustainable, green energy production/storage [5].

A current challenge RFBs face is their relatively low energy density trait [5]. Improving the energy density by optimizing the electrolyte is key to improving RFB technology. Various chemistries have been tested to this effect (Fe/Cr [6], Zn/Br [7–9], V/V [10–12], and V/Br [13]). Of these chemistries, V/V or all-vanadium chemistry is the most widely studied and applied and is particularly attractive due to the lack of negative effects caused by cross-contamination of active species [10]. Vanadium redox flow batteries (VRFBs), like other traditional redox flow batteries, use two liquid electrolytes to facilitate the redox reaction and store/release energy as required. This is accomplished through the use of four oxidation states of vanadium (V^{2+}, V^{3+}, VO^{2+} (otherwise V^{4+}), and VO_2^+ (otherwise V^{5+})). The redox pairs are stored in separate tanks and circulated through separate half-cells of the battery (shown in Fig. 1). V^{5+}/V^{4+} flow through the positive half-cell, and V^{2+}/V^{3+} flow through the negative half-cell.

During the charging process, blue V^{4+} ions release an electron and are oxidized to yellow V^{5+}; the reverse is true while discharging. A proton is transferred through the membrane where a V^{3+} ion accepts the electron and is reduced to V^{2+}. This process is shown in Fig. 2. The negative and positive half-cell reactions are shown in the following equations, Eqs. (1) and (2), while the overall discharge reaction is shown below in Eq. (3). When the system is in a discharged state, the negative and positive electrolytes contain only V^{3+} and V^{4+} (VO^{2+}). Rather while in the charged state, the negative electrolyte is reduced to V^{2+}, while the positive electrolyte is oxidized to V^{5+} (VO_2^+) [14].

Positive cell reaction:

$$VO_2^+ + 2H^+ + e^- \rightleftharpoons VO^{2+} + H_2O \quad (1)$$

[1]Corresponding author.

Manuscript received October 22, 2019; final manuscript received March 19, 2020; published online April 9, 2020. Assoc. Editor: Leela Mohana Reddy Arava.

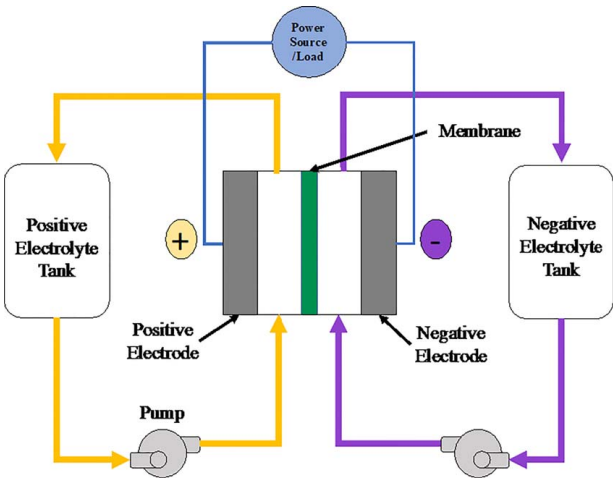

Fig. 1 Redox flow battery diagram

Negative cell reaction:

$$V^{2+} \rightleftharpoons V^{3+} + e^{-} \tag{2}$$

Overall discharge reaction:

$$VO_2^{+} + V^{2+} + 2H^{+} \rightleftharpoons VO^{2+} + V^{3+} + H_2O \tag{3}$$

Vanadium chemistry was used in this work to develop a proof-of-concept cell design template which can be used for future studies with varying chemistries. To the authors' findings, there is little reported literature on the design, preparation, and testing of a simple, low-concentration VRFB for preliminary research. This study aims to fill that gap and thereby broaden the accessibility of the technology. The paper is organized as follows. Section 2 provides an overview of the literature related to vanadium redox flow batteries and a summary of the electrolyte, membrane, electrode, and peripheral battery components. The experimental procedure and corresponding results are shown in Secs. 3 and 4, respectively. A computational study is performed in Sec. 5, and the results are discussed and compared with the experimental results in Secs. 6 and 7. Section 8 the paper is then concluded, and future work is discussed.

2 Literature Review

A VRFB has four main components that compose its structure: the electrolyte, electrode, membrane, and bipolar plate. Additionally, the gaskets, collector plates, end plates, and pumps must be considered. The electrolyte in a VRFB is crucial to the energy storage capability of the battery. Since the electrolyte storage is kept separate from the battery stack, the capacity and power bank of a flow battery can be independently scaled. The typical limiting factor of flow batteries, however, is the energy density: this is dependent on the concentration of the active species in the electrolyte. The other components provide structure to the battery and allow transport of electrons between the stack and the external circuit. A VRFB's membrane is intended to inhibit cross mixing of opposing electrolytes while allowing ion exchange to occur.

Particularly, important traits of the membrane include high ion conductivity, high chemical stability, and good ion selectivity. Chemical stability in the membrane is necessary for ensuring a prolonged lifespan of the battery, while high proton conductivity and ion selectivity are required for increasing the efficiency of the battery. The latter two traits allow for the completion of the internal circuit, and to inhibit cross-contamination and resulting self-discharge, respectively [15]. The electrode acts as a catalyst for the oxidation and reduction reactions that occur within the cell while also completing the electrical connection between the membrane and bipolar plate. For this, the electrode requires a high reactive surface area while also permitting ample electrolyte flow through the cell and maintaining low electrical resistance and chemical reactivity. Porous forms of carbon (felt [16], paper [17], and cloth [18]) are thus typically used. The bipolar plates are akin to the poles of a standard battery cell. These graphite plates are the cell's connection to the external electrical circuit and act to separate adjacent cells in a stack of cells. In a discharge cycle, electrons released from the negative half-cell are collected by the bipolar plate and are transferred to the positive half-cell; the reverse is true while the battery is charging. The bipolar plate is required to have a high electrical conductivity and low chemical reactivity to extend the life span of the cell. Electrolyte flow paths are often cut into the bipolar plate to reduce the pressure drop through the porous electrode. Sections 2.1–2.7 describe different components of RFB and related researches.

2.1 Electrolyte. With the all-vanadium chemistry, the concentration of vanadium is typically limited to 2 M in commercial applications due to the relatively low solubility of the range of vanadium ions in the supporting electrolyte [19]. This low solubility is

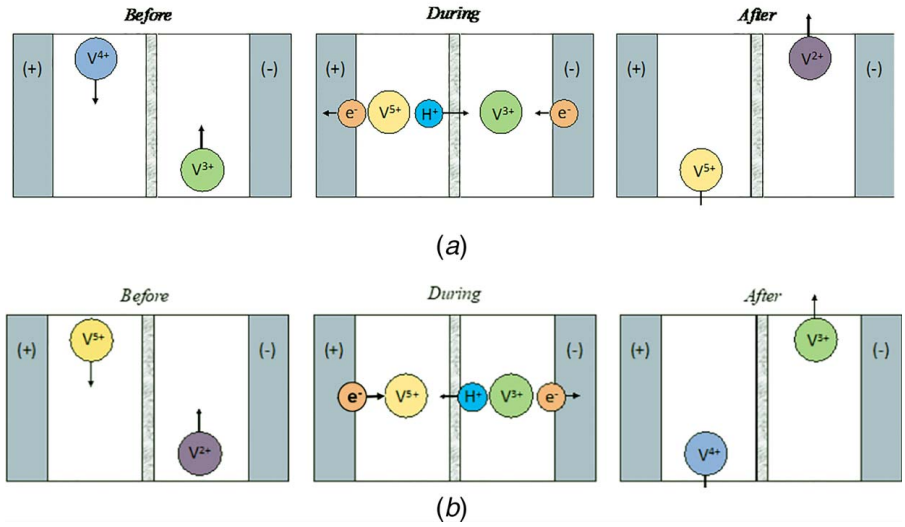

Fig. 2 (*a*) Charging and (*b*) discharging process depictions of a VRFB

especially apparent at high temperatures (above 40 °C) for vanadium (V) and low temperatures (below 5 °C) for vanadium (II) and (III) [19]. There are numerous studies on improving the concentration with supersaturated solutions [20], additives [21–24], and other contributors for chemical stability [20] as well as alterations to the electrolyte chemistry [19,25–28]. The electrolyte used in this experimental work is composed of 0.066 M vanadium pentoxide and 2 M sulfuric acid.

2.2 Membrane. There are two commonly used membranes: ion exchange membranes (IEMs) and nanofiltration membranes. IEMs selectively allow ions to pass through based on the ion's charge and whether the membrane is anionic or cationic [29], while nanofiltration membranes utilize geometry to impede the exchange of larger ions like vanadium while allowing smaller ions like hydrogen to pass [30]. Membrane research currently relates to improving ion selectivity while reducing the overall cost of the materials, which is a significant contribution to the limitation of flow battery commercialization [30]. The membrane used throughout the experimental procedure is a VANADion™ membrane: an IEM developed by DuPont with a thickness of 254 μm.

2.3 Electrode. The field of electrode research contains various work improving performance using thinner electrodes [17], heat treatments [31–33] and other surface treatments [34–38], structural modifications [39], new materials [40–42], and reducing contact resistance with compression [43,44]. Despite the porosity, the high compressions required for optimal electrical conductivity tend to cause a large pressure drop across the electrode. The electrodes in this work are graphite felt with a total uncompressed thickness of 9 mm.

2.4 Bipolar Plate. There have been many studies (experimental [45], mathematical [46,47], or a combination [48,49]) comparing conventional, parallel, interdigitated, and serpentine flow fields for use in VRFBs, though the optimal choice is ultimately dependent on the scale of the battery being constructed. These flow fields are depicted in Fig. 3. The ideal path is one that minimizes electrical shunt currents while still minimizing the pressure drop [50].

Further bipolar plate research is conducted to improve the material properties. By using carbon composites instead of plain graphite, the dissolution of the plates into the electrolytes could be prevented [51]. Additives like carbon black used by Lee et al. [51] and ketjenblack nanoparticles used by Park et al. [52] showed comparable or improved efficiencies to regular graphite while also improving the chemical stability in the acidic electrolyte. There has also been success in bipolar plates without carbon, such as an IrO_x coated TiO_2 plate developed by Han et al. [53]. The bipolar plates used for this design are plain graphite plates with a thickness of 2.8 mm.

2.5 Gasket. Gaskets are crucial for the structural integrity and functionality of the VRFB cell/stack. Most commonly, polytetrafluoroethylene (PTFE), polyvinyl chloride (PVC), and silicone are used as gasket materials; the material used and overall gasket design depend on the required cell compression.

2.6 Current Collector Plate. Current collectors are similar in function to bipolar plates but are typically made from a highly conductive metal like copper and are placed only at the ends of the stack. The simplicity of a single cell design often allows the function of the metallic plate to be performed by the bipolar plate, so the term is sometimes used to describe either. The experimental cell described in this work did not use a current collector. As a single cell configuration, the external wiring was attached directly to the bipolar plate.

2.7 Pumps. Due to the acidic nature of the electrolyte, peristaltic pumps are often used for electrolyte circulation to avoid electrolyte contact with mechanical components. With this, an optimal flowrate is crucial to the efficiency of a VRFB. Tang et al. [50] and Ma et al. [54] show the benefits of variable flowrates, particularly toward the end of charging and discharging cycles, which tend to improve efficiencies. The electrolyte flow direction is also important; having the electrolytes enter the battery cells from opposing directions allows for similar drops in electrolyte charge among cells, which improves operating conditions [55].

3 Experimental Procedure

This section describes the experimental procedure, materials used, design, and development of different components, followed by the assembly and preparation of a VRFB.

3.1 Materials

3.1.1 H-Cell. An H-cell is an electrolysis cell with two half-cells that is used to charge either one or both electrolytes at a time. The H-cell was used in this application in order to reduce the exposure time of the electrolyte within the cell. The acidic and destructive nature of the sulfuric acid within the electrolyte can damage the membrane and gaskets throughout the cell, compromising the end results. The two half-cells are separated such that there is no direct mixing of the contents in each half cell, but a transfer of protons can still occur. The concept of this is illustrated in Fig. 4 and the implementation in Fig. 5. A VANADion™ membrane was used in the present design. Size 2 PVC pipe, T-connections, flanges, and end caps (McMaster-Carr) were used to assemble the H-cell reservoirs. The PVC material was chosen for this due to its resistance to degradation with sulfuric acid and its low cost. Silicone gasketing was used to seal the two reservoirs together between the membranes. Two electrodes were cut from the stock graphite used for the bipolar plates and were attached to an INSTEK laboratory DC power supply during operation. Rubber was wrapped around the electrodes to prevent the electrical contact between the electrodes and supports; the electrodes were then suspended in the H-cell reservoirs. The process of charging the electrolyte in the H-cell took longer than charging within the battery due to the low electrical conductivity created from the gap between the positive and negative electrode, but this time tradeoff was deemed beneficial due to the lesser cell damage applied.

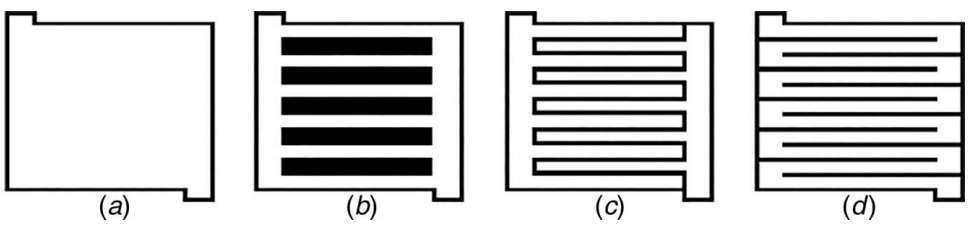

Fig. 3 (*a*) Conventional, (*b*) parallel, (c) interdigitated, and (*d*) serpentine flow fields

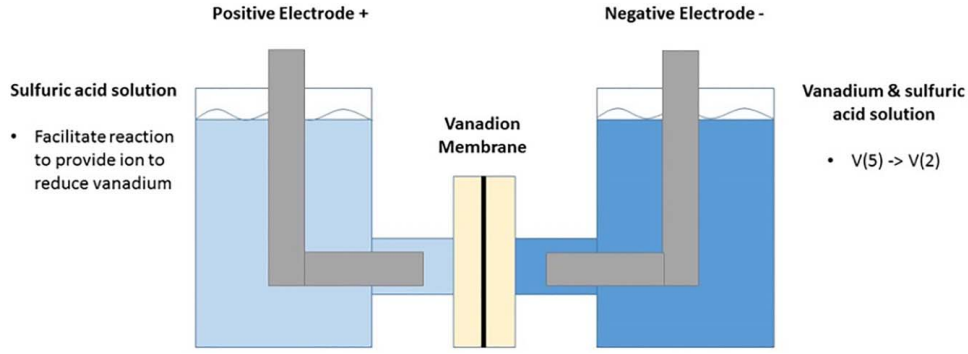

Fig. 4 Description of the electrolysis process

3.1.2 Battery Cell and Electrolyte. 0.066 M of vanadium pentoxide (+98%) and 2 M sulfuric acid (Fisher Scientific) in de-ionized water composed the electrolyte. This amount of vanadium was chosen due to the solubility limit of the element. All components were added and stirred in a beaker using a Fisher Scientific magnetic stirrer. The solution was stirred until all vanadium was fully dissolved as shown in Fig. 6. Graphite sheets (2.8 mm thickness, TDM FuelCellStore) were cut to 10 cm × 10 cm for use as the bipolar plate (Fig. 7(*a*)). Holes were drilled and filled with silicone for the electrolyte to flow in to the half-cell. These pathways will prevent the electrolyte contact with the graphite plate, improving the component's life. Silicone gasketing (3 mm thickness, Apple Silicone USA, shown in Fig. 7(*b*)) was used to separate the bipolar plate and the membrane, providing a gap for the electrode to reside. This was compressed against a PTFE flow frame (MTI Corporation) used to distribute the electrolyte. The PTFE flow frame used is shown in Fig. 7(*c*). It possesses an active area of 7 cm × 7 cm and was 2.1 mm thick.

Graphite felt (FuelCellStore, shown in Fig. 7(*d*)), placed in series, was used for the electrode. In this setup, two electrodes with thicknesses of 2.5 mm and 6.5 mm were placed in series to achieve this thickness. The total, uncompressed thickness of each electrode segment was 9 mm in order to obtain sufficient compression once assembled.

A VANADion™ membrane (Nafion™ Store) was used as a separator. This membrane was cut into a 10 cm × 10 cm square, a larger area than the 7 cm × 7 cm active area to ensure proper adhesion against the silicone seals. Two PVC endplates (McMaster-Carr) were used as inlets/outlets for the electrolyte, for binding the cell together and applying compression. The entire assembly was held together with 16 threaded rods. This is shown below in Figs. 8(*a*) and 8(*b*). Two peristaltic pumps (OEM 206, CR pump) were used to circulate the electrolyte at an arbitrary flowrate of 200 mL/min for all tests. The pumps can be seen below in Fig. 9.

3.2 Cell Design. Figure 10 depicts an exploded view of the SolidWorks cell model. The cell utilizes a conventional flow through configuration, implying that the electrolyte comes through the inlet, is forced through the electrode then out through the outlet.

3.3 Assembly and Preparation. The electrolytes were initially prepared using the H-cell. A low-concentration vanadium solution composed of 6 g V_2O_5 dissolved in 1 L of 2 M H_2SO_4 (approximately 0.066 M vanadium) was poured in the negative half-cell such that the membrane was fully covered (450–500 mL), and the same volume of 4 M sulfuric acid was added to the positive half-cell. The power supply terminals were connected

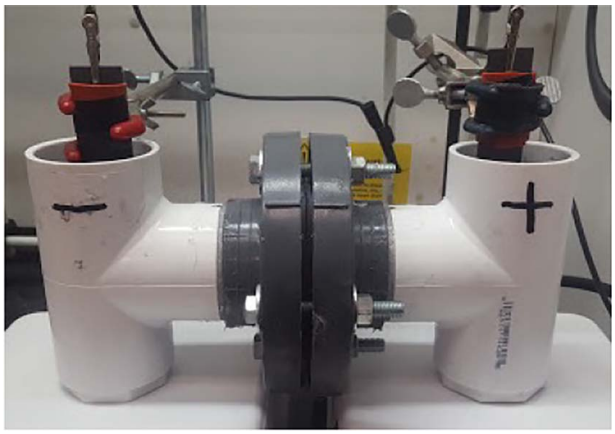

Fig. 5 H-cell during the electrolyte charge process

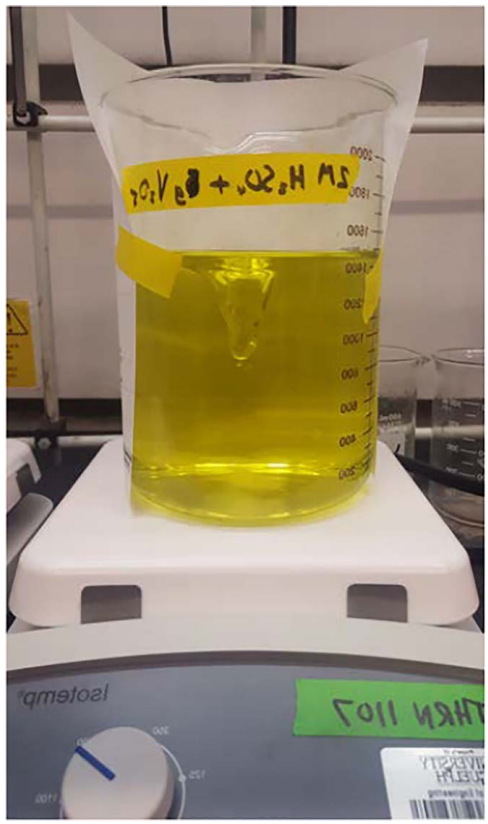

Fig. 6 Electrolyte (vanadium V) solution during the stirring process

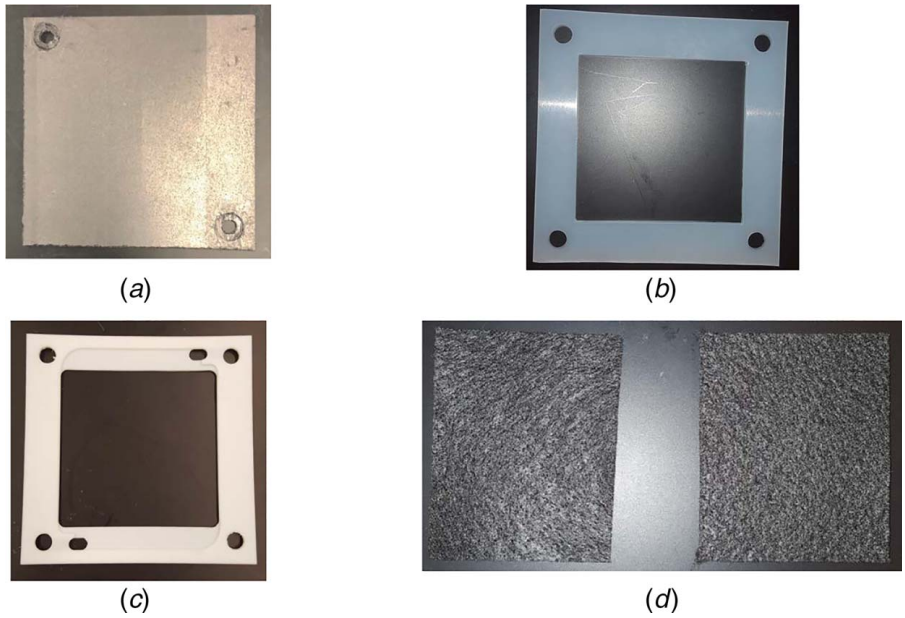

Fig. 7 Components used in the battery stack: (*a*) graphite bipolar plate, (*b*) silicone gasket, (*c*) PTFE flow frame, and (*d*) carbon felt electrodes

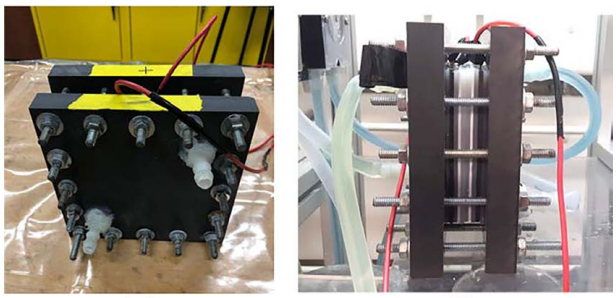

Fig. 8 (*a*) Front assembled view of the cell's endplate and (*b*) side assembled view of the cell

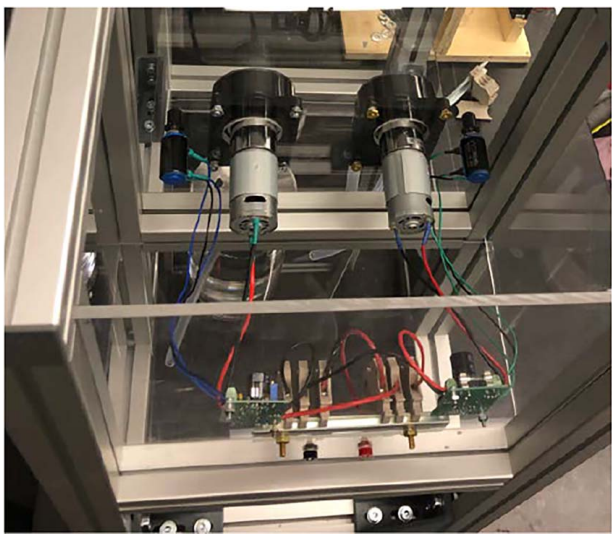

Fig. 9 Top view of peristaltic pumps and the pumps electrical

to the appropriate electrodes, and 1.6–1.8 V was applied across the graphite rods. An electrolyte solution of V^{3+} and another electrolyte solution of V^{4+} were created separately after leaving the h-cell with the applied voltage for many hours. The states of the electrolyte throughout all experiments were determined through visual indication; as V^{5+} is yellow in color, V^{4+} is blue, V^{3+} is green, and V^{2+} is violet [56,57]. The separate V^{3+} and V^{4+} solutions were then run through the flow battery cell and charged fully (to the V^{5+} and V^{2+} states) applying a voltage of 1.8 V. Approximately 50 mL of the electrolyte remained in each half cell and tubing while the cell was operating, leaving 400 mL of solution in each storage reservoir.

4 Experimental Results

4.1 Polarization Curve. Using a range of resistors between 1 Ω and 10 kΩ, the cell's output voltages were measured and plotted against the calculated currents to create the polarization curve in Fig. 11. The short circuit current was measured with a multimeter. All measurements were taken at an approximate full state of charge, and the steady-state voltage was recorded across each resistor. The state of charge was determined through the spike in voltage reading during the charging process along with the color state of each electrolyte. Through a deep and extended, charging and discharging cycle, the colors of the electrolytes would change, giving us a supplementary visual indication. The experimental polarization curve shows an activation polarization drop of approximately 0.16 V before ohmic losses dominate above 3 mA/cm^2. Limitations in equipment restricted measurements at higher current densities, so a curve was fitted to provide an estimate of this region. Evidently, increased mass transport losses above current densities of 20 mA/cm^2 are likely due to the low active species concentration. It is speculated that the overall performance is also dominated by concentration losses, which could cause the short circuit current density <35 mA/cm^2.

4.2 Charge/Discharge Studies. A high-resolution computerized battery analyzer (CBA HR, West Mountain Radio) was acquired to perform discharge tests with a controlled current. Charge tests were performed with a DC power supply and multimeter for monitoring the current; the charge data were collected with

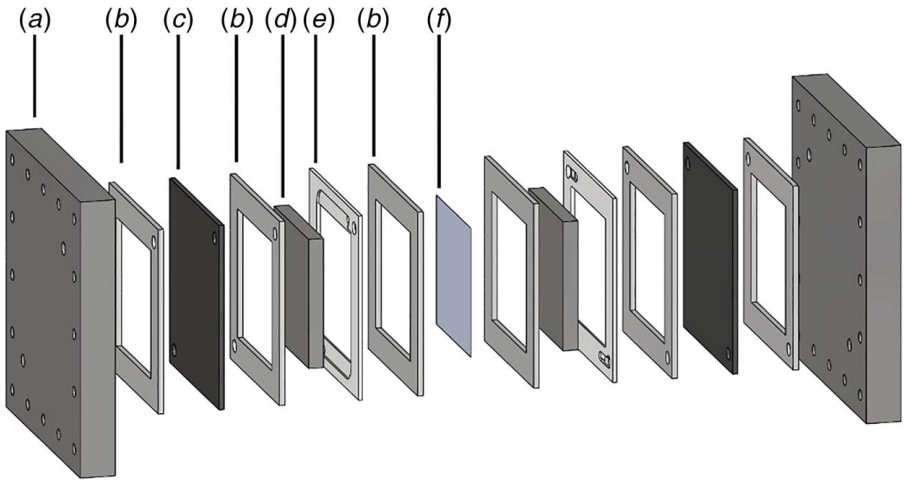

Fig. 10 SolidWorks assembly of individual cell components: (*a*) endplate, (*b*) silicone gasket, (c) bipolar plate, (*d*) graphite felt, (e) PTFE flow frame (MTI Corporation), and (*f*) VANADion™ membrane

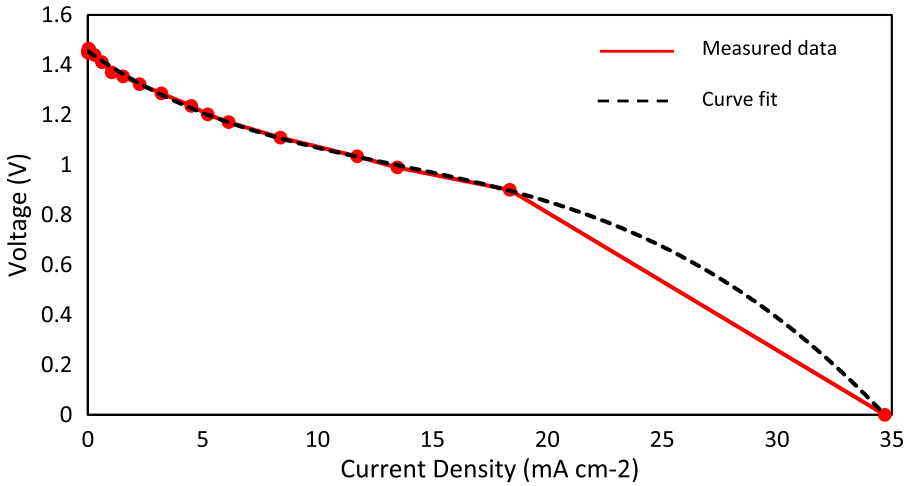

Fig. 11 Polarization curve of VRFB

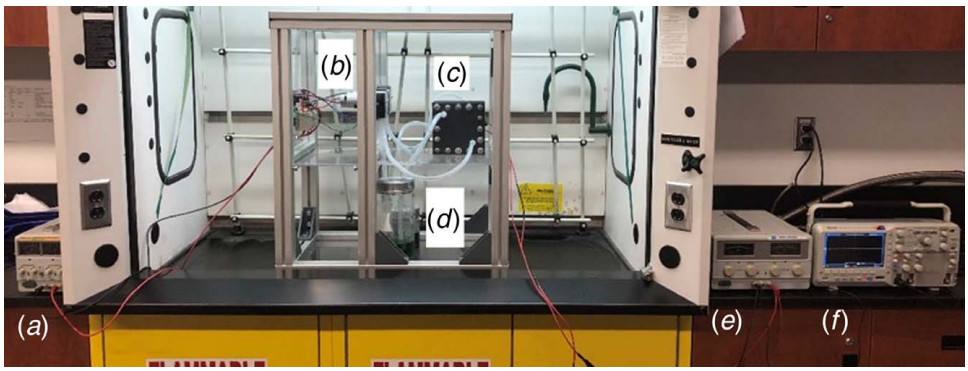

Fig. 12 Experimental charging setup with (*a*) motor power supply, (*b*) motor circuitry, (*c*) battery cell and auxiliary tubing, (*d*) electrolyte storage tanks, (*e*) charging power supply, and (*f*) oscilloscope for data acquisition

an oscilloscope. Figure 12 depicts the charging experimental configuration.

Figure 13 shows the charge/discharge curves at four different current values between 500 mA and 800 mA (10.20–16.33 mA/cm^2) produced by the created VRFB. The cutoff voltage for the discharge tests was limited by the equipment and set to 0.5 V; charge tests were run until both electrolytes visually appeared to be in their charged oxidation states. The cell's discharge voltage remains relatively level throughout the course of both the 12.24 and 14.29 mA/cm^2 discharge tests.

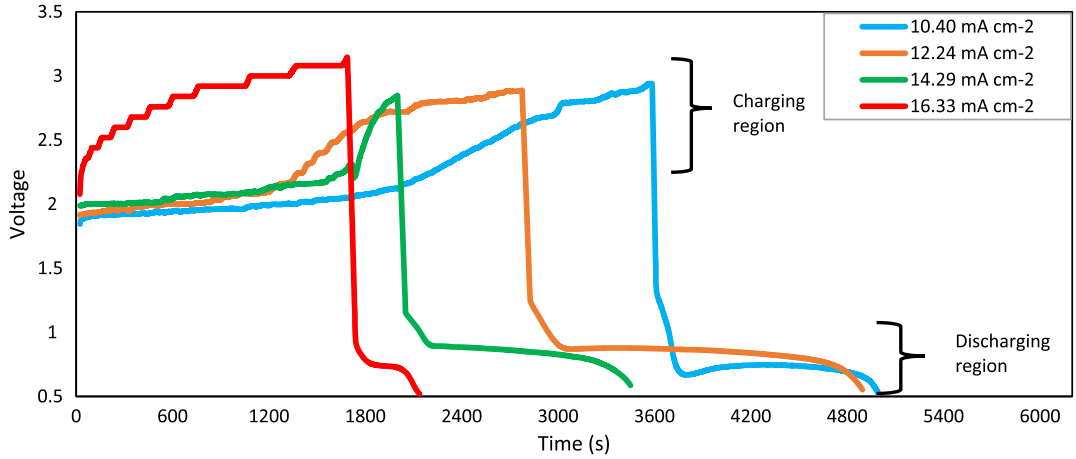

Fig. 13 Voltage versus time charge/discharge plots for 10.20, 12.24, 14.29, and 16.33 mA/cm^2

4.3 Efficiency. The voltage, coulombic, and energy efficiencies (η_V, η_C, and η_E, respectively) were calculated with Eqs. (4)–(6), respectively, for each of the currents tested

$$\eta_V = \frac{\int V_{\text{Discharge}}\,dt}{\int V_{\text{Charge}}\,dt} \times 100 \approx \frac{V_{\text{Discharge},Avg}}{V_{\text{Charge},Avg}} \times 100 \tag{4}$$

$$\eta_C = \frac{\int I_{\text{Discharge}}\,dt}{\int I_{\text{Charge}}\,dt} \times 100 = \frac{t_{\text{Discharge}}}{t_{\text{Charge}}} \times 100 \tag{5}$$

$$\eta_E = \eta_V \times \eta_C \tag{6}$$

Table 1 Efficiencies of experimental VRFB at four current densities

Current (mA)	Current density (mA/cm^2)	Voltage efficiency (%)	Coulombic efficiency (%)	Energy efficiency (%)
500	10.20	31.46	78.52	24.70
600	12.24	35.12	76.31	26.80
700	14.29	39.36	72.44	28.51
800	16.33	25.69	26.59	6.83

Table 1 and Fig. 14 show the voltage, coulombic, and energy efficiencies for each of the tested current densities. Despite the increased voltage efficiency at lower current densities, it is evident that the overall efficiency is higher between 12.24 and 14.49 mA/cm^2. It is to be expected that the voltage efficiency is higher at lower current densities since the discharge and charge voltages are higher and lower, respectively, as shown in Fig. 13. At higher current densities, the required voltages diverge. However, the current efficiency is decreased at lower current densities likely because the difference in the time required to fully charge and discharge becomes greater. The efficiency shows to rapidly reduce between the 14.29 mA/cm^2 and the 16.33 mA/cm^2 tests; it is hypothesized that this represents a limit due to the low concentration.

5 Computational Procedure

A computational model of a single cell VRFB is developed in order to compare the results obtained from the experimental setup. Cell running parameters can be adjusted in the model to see the output effects without having to run the battery.

The computational model takes into consideration the following components: the positive electrolyte, the negative electrolyte, the positive electrode, the negative electrode, and the ion exchange

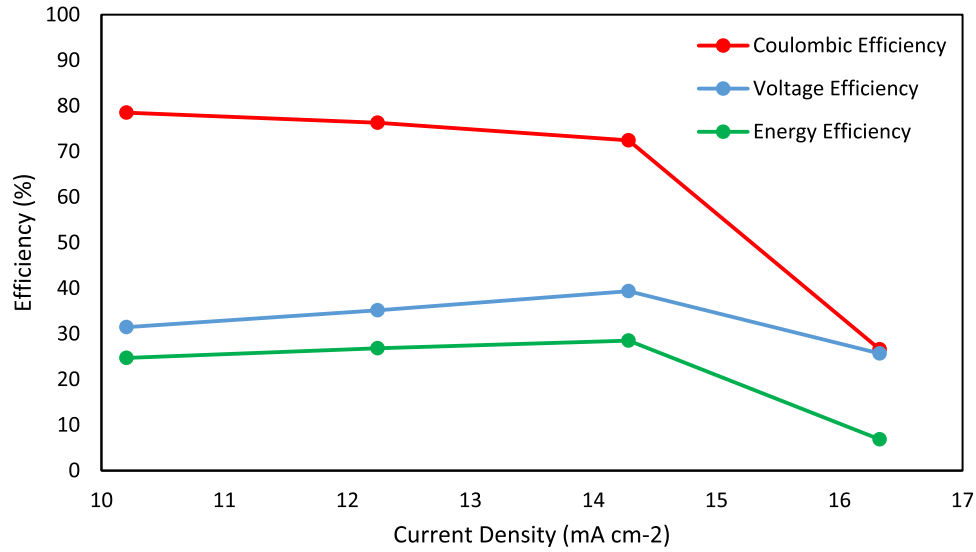

Fig. 14 Voltage, coulombic, and energy efficiencies of experimental VRFB

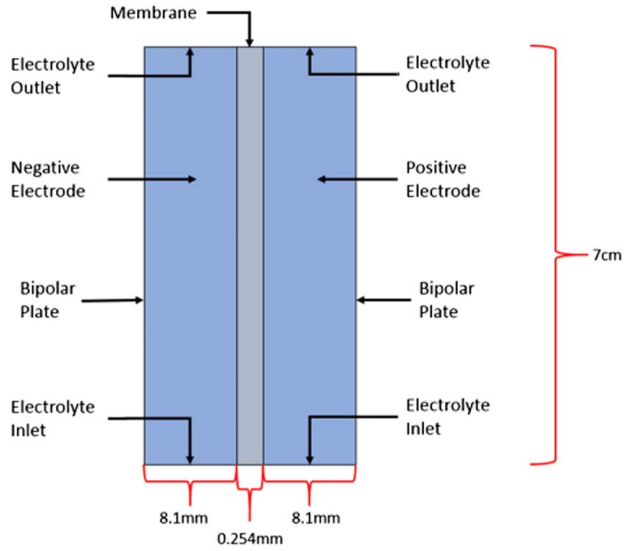

Fig. 15 2D model schematic diagram

membrane, all shown in Fig. 15 (Note: the above figure is not to scale). The bipolar plate was not considered in this model. Governing equations have been formed for each component and will be discussed in Sec. 5.1.

5.1 Model Equations

5.1.1 Electrolyte and Electrode Reaction Equations. Two steps of dissociation of the sulfuric acid to sulfate occur during the operation of the battery. This occurs due to the water content in the electrolyte

$$H_2SO_4 \rightarrow H^+ + HSO_4^- \tag{7}$$

$$HSO_4^- \rightarrow H^+ + SO_4^{2-} \tag{8}$$

Equations (7) and (8) can be characterized using the following formula, in order to account for changes in concentrations during the two stages of dissociation [58,59]

$$r_d = k_d\left(\frac{\alpha_{H^+} - \alpha_{HSO_4^-}}{\alpha_{H^+} + \alpha_{HSO_4^-}} - \beta\right) \tag{9}$$

The reaction at equilibrium can be modeled from the Nernst equation shown below [58], governing the potential of the positive and negative half-cells due to the Nernst equation, respectively

$$E = E_{0,Pos} + \frac{RT}{nF}\ln\left(\frac{C_{V^{5+}}\cdot(C_{H^+})^2}{C_{V^{4+}}}\right) \tag{10}$$

$$E = E_{0,Neg} + \frac{RT}{nF}\ln\left(\frac{C_{V^{3+}}}{C_{V^{2+}}}\right) \tag{11}$$

In the above equations, the value of R is 8.31 J/(mol K) and F is 96,485 A/mol, $C_{V^{2+}}$ is the concentration of V^{2+} (mol/m^3), $C_{V^{3+}}$ is the concentration of V^{3+} (mol/m^3), $C_{V^{4+}}$ is the concentration of V^{4+}(mol/m^3), $C_{V^{5+}}$ is the concentration of V^{5+} (mol/m^3), and C_{H^+} is the concentration of H^+ (mol/m^3).

For the determination of the cell current, the Butler–Volmer equation [58,60] is used to draw the relationship between the electrode properties and the current produced in the positive and negative side, respectively

$$i_{pos} = AFk_{pos}(C^e_{V^{4+}})^{(1-\alpha_{pos})}(C^e_{V^{5+}})^{(\alpha_{pos})} \times\left[\left(\frac{C^s_{V^{4+}}}{C^e_{V^{4+}}}\right)\exp\left(\frac{1-\alpha_{pos}F\eta_{pos}}{RT}\right) - \left(\frac{C^s_{V^{5+}}}{C^e_{V^{5+}}}\right)exp\left(\frac{1-\alpha_{pos}F\eta_{pos}}{RT}\right)\right] \tag{12}$$

$$i_{neg} = AFk_{neg}(C^e_{V^{2+}})^{(1-\alpha_{neg})}(C^e_{V^{3+}})^{(\alpha_{neg})} \times\left[\left(\frac{C^s_{V^{2+}}}{C^e_{V^{2+}}}\right)\exp\left(\frac{1-\alpha_{neg}F\eta_{neg}}{RT}\right) - \left(\frac{C^s_{V^{3+}}}{C^e_{V^{3+}}}\right)\exp\left(\frac{1-\alpha_{neg}F\eta_{neg}}{RT}\right)\right] \tag{13}$$

The electrochemical overpotential variable can be defined and calculated for the positive and negative side as follows [52]:

$$\eta_{pos} = \phi_s - \phi_l - E_{eq,pos} \tag{14}$$

$$\eta_{neg} = \phi_s - \phi_l - E_{eq,neg} \tag{15}$$

The catalytic performance of the electrodes governs the overall electrochemical performance of the redox flow battery cell. The overall system power is calculated by the reaction rate of the redox species involved (at the electrode) and the associated surface area of the electrode [37]. In order to maximize the output power, the total area/surface area of the electrode must be considered and expanded accordingly [15]. This is one of the reasons why highly porous materials with large surface areas such as graphite felt and carbon structures are used for this component.

5.1.2 Ion Transport Equation. In order to take into consideration of the concentration changes, the Nernst–Planck equation can be used to calculate the total flux via diffusion [54]

$$\mathbf{N}_i = -D_i^{eff}\nabla C_i - \frac{z_i F}{RT}C_i D_i^{eff}\nabla\phi_l + \mathbf{v}C_i \tag{16}$$

Calculating the total current density in the electrolyte can be done using the following equation [60]:

$$\mathbf{i} = \sum_i \mathbf{i}_i = \frac{F^2}{RT}\nabla\phi\sum_i z_i^2 D_i^{eff} c_i - F\sum_i z_i D_i^{eff}\nabla c_i \tag{17}$$

where $\mathbf{i}$ is the current density in the electrolyte.

Due to the nature of the membrane, a charge will exist within the component that must be included to further the model accuracy. This is accounted for in the following equation [54]:

$$\rho_{fix} + F\sum_{i=1}^{n} z_i c_i = 0 \tag{18}$$

where ρ_{fix} is the fixed charge from the membrane.

Table 2 Sensitivity analysis of model

State of charge	Number of elements						
	5871	4616	3511	2556	1196	314	176
10	1.3202	1.3202	1.3202	1.3202	1.3202	n/a	n/a
15.15	1.3352	1.3352	1.3352	1.3352	1.3352	n/a	n/a
20	1.3471	1.3471	1.347	1.347	1.347	n/a	n/a
30	1.3683	1.3683	1.3683	1.3683	1.3683	1.3869	1.3869
40	1.3878	1.3878	1.3878	1.3878	1.3878	1.3869	1.3869
50	1.4074	1.4074	1.4074	1.4074	1.4074	1.4065	1.4065
60	1.4286	1.4286	1.4286	1.4286	1.4286	1.4277	1.4277
70	1.4537	1.4537	1.4537	1.4537	1.4537	1.4528	1.4528
80	1.4873	1.4873	1.4873	1.4873	1.4873	1.4863	1.4863
84.85	1.5103	1.5103	1.5103	1.5103	1.5103	1.5092	1.5092
90	1.5461	1.5461	1.5461	1.5461	1.5461	1.5446	1.5446

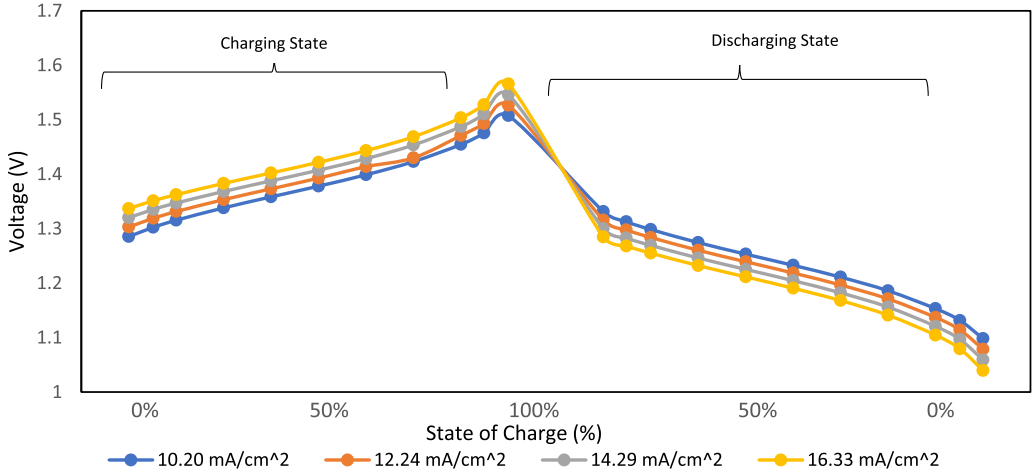

Fig. 16 Simulation model potential of the charge and discharge cycle

5.1.3 Membrane Equations. To effectively model the concentration and potential shifts at the membrane and electrolyte interface, the Donnan equation can be used [52]

$$\Delta\phi = \frac{RT}{F}\ln\left(\frac{c_c^e}{c_c^m}\right) \tag{19}$$

5.1.4 Model Parameters. The model created replicating the geometry shown in Fig. 15 used a total of 4616 elements over the three components. An average mesh quality of 0.9733 was generated with the chosen element parameters, indicating a strong mesh. In order to further test the models sensitivity, a sensitivity analysis was performed in Table 2. The results show that the model converged quickly. Reviewing the data below, the values converged quickly over the 3511 element mark. In setting the boundary conditions for the model, the negative electrode was grounded. A constant current density was to be selected as desired. The model created is to represent a 2D (as displayed in Fig. 15) approximation. Due to the 2D design of this model, any parameter variation in the z direction (third dimension) is neglected. Fluid flow throughout the cell is treated and assumed to be incompressible and steady. Volume changes resulting from the multiple reactions (and unwanted side reactions) are ignored in these calculations. All reactions/transactions within the cell are isothermal. Any hydrogen and oxygen evolution reactions within the cell are neglected within this model. This point is to be considered as a limitation of the model as gas evolution may occur during the reaction. The parameters were modeled off of the values provided in the stock vanadium redox flow battery COMSOL model. The parameters were then adjusted to further suit the created VRFB for better overall accuracy.

6 Computational Results

Figure 16 shows the output from the modified COMSOL vanadium redox flow battery model. The model was produced using the parameters from Table 3, with a state of charge of 90% and a current density of 14.29 mA/cm^2. It is important to note the current density value used in this model and obtained from our created cell is smaller than other common experimental setups seen in the literature. This is largely accredited to the low concentration of vanadium within the electrolyte. Most laboratory setups use vanadium concentrations around 2 M, where our setup was limited to 0.066 M of vanadium. The current density of 14.29 mA/cm^2 was chosen for the model output results section as a result of the Sec. 5.3 efficiency. This was the optimum case with the highest net efficiency.

Table 3 Model parameters

Value	Description
9.312×10^{-9} m^2/s	H(+) diffusion coefficient
7×10^{-8} m/s	Rate constant, negative reaction
6.9 S/m	Electrode conductivity
6.6 mol/m^3	VO(2+) initial concentration
6.6 mol/m^3	V(3+) initial concentration
59.4 mol/m^3	VO2(+) initial concentration
59.4 mol/m^3	V(2+) initial concentration
4.9×10^5 L/m	Electrode specific area
40 A/m^2	Average current density
0.0088183 m/s	Inlet velocity
3.9×10^{-10} m^2/s	VO2(+) diffusion coefficient
3.9×10^{-10} m^2/s	VO(2+) diffusion coefficient
293.15 K	Cell temperature
2000 mol/m^3	$HSO_4(-)$ initial concentration, positive electrode
2000 mol/m^3	$HSO_4(-)$ initial concentration, negative electrode
2000 mol/m^3	H(+) initial concentration, positive electrode
2000 mol/m^3	H(+) initial concentration, negative electrode
2.5×10^{-8} m/s	Rate constant, positive reaction
2.54×10^{-4} m	Membrane thickness
2.4×10^{-10} m^2/s	V(3+) diffusion coefficient
2.4×10^{-10} m^2/s	V(2+) diffusion coefficient
10,000 mol/(m^3 s)	$HSO_4(-)$ dissociation rate constant
1990 mol/m^3	Membrane proton concentration
1.33×10^{-9} m^2/s	$HSO_4(-)$ diffusion coefficient
1.065×10^{-9} m^2/s	$SO_4(2-)$ diffusion coefficient
1.004 V	Standard potential, positive reaction
0 mol/m^3	(0[M] used during current distribution initialization, −cHm used after auxiliary sweep)
0.55	Transfer coefficient, positive reaction
0.45	Transfer coefficient, negative reaction
−0.255 V	Standard potential, negative reaction
0.25	Dissociation constant
0.07 m	Cell depth
0.07 m	Cell height
0.0081 m	Electrode thickness
0.93	Electrode porosity

The state of charge noted through this section is reflected through the vanadium initial concentration values. Figure 16 varies the state of charge value across four different current densities, plotting the results for a complete charge and discharge cycle. The curve in Fig. 16 displays the theoretical charging and discharging voltages throughout the batteries' state of charge. Under all current density conditions, the charge/discharge voltages trended similarly. As the charge/discharge current increased, the charging voltage increased and discharging voltage reduced, suggesting the voltage efficiency reduces in our model as the current density increases.

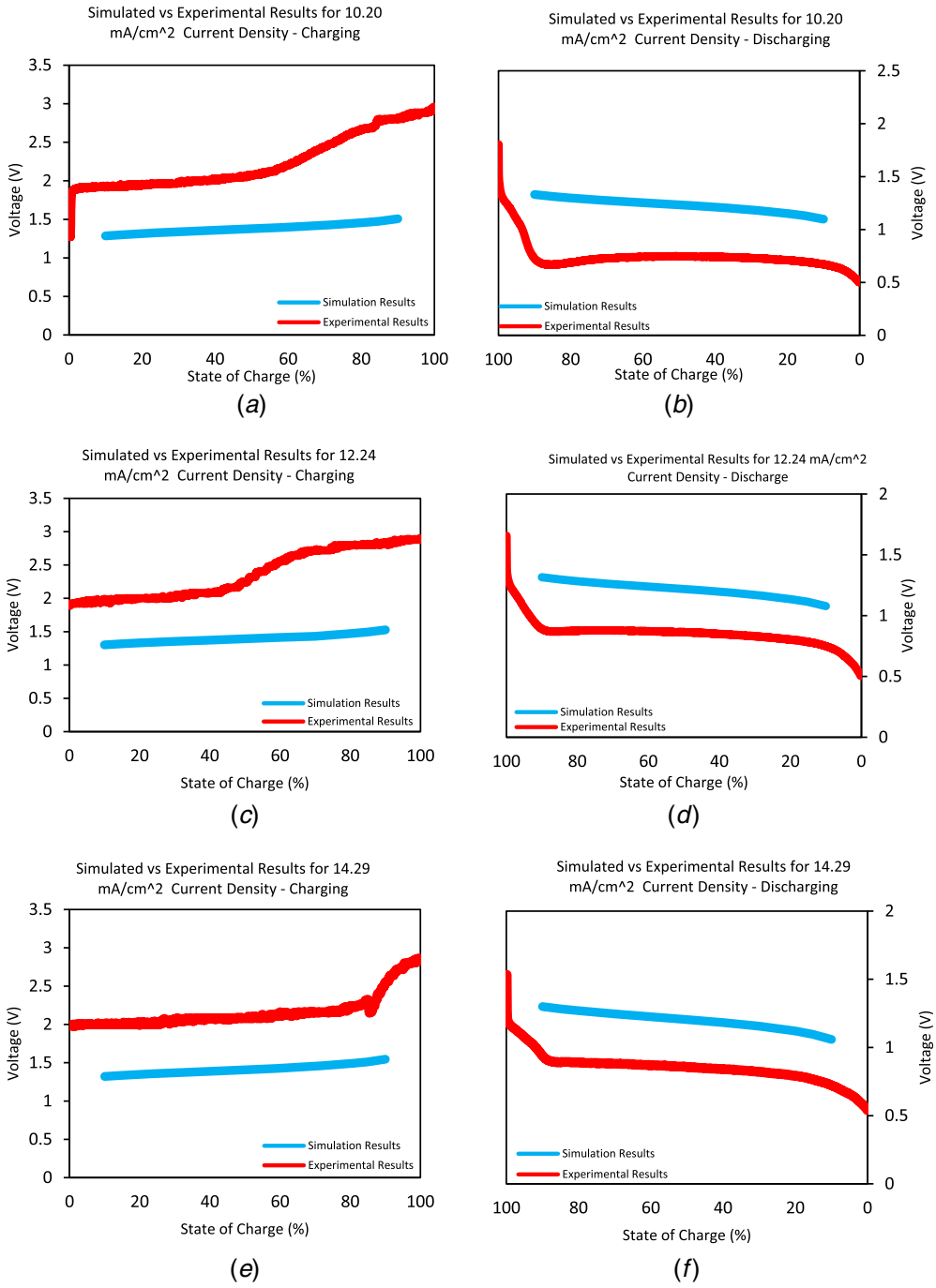

Fig. 17 Experimental results versus simulation results at: 10.20 mA/cm^2 (*a*) charging; (*b*) discharging; 12.24 mA/cm^2 (*c*) charging, (*d*) discharging; and 14.29 mA/cm^2 (*e*) charging, and (*f*) discharging

7 Experimental Versus Computational Results

Figures 17(*a*)–17(*f*) show the experimental and simulation output voltage versus state of charge plots. Due to the nature of the model, the state of charge could not be computed lower than 10% or higher than 90%, and this is reflected amongst the plots. As expected, the experimental voltages were higher than the simulation voltages during the charging cycle, and the experimental voltages were lower than the simulation voltages during the discharge cycle. The large discrepancy between the two datasets is believed to be because of the large losses associated with our setup and the low concentration of vanadium in the two electrolytes.

As predicted in the model, the voltages during charging and discharging were higher and lower, respectively, at higher current densities. This was reflected in the experimental results, though the effects were more drastic. A very noticeable drop in experimental performance was observed between tests.

8 Conclusion

The successful creation of a VRFB electrolyte and the design/construction of a VRFB cell have been outlined in this paper. It serves as a proof of concept for the cell design and testing methods. Of the tested current densities, the VRFB showed a highest overall efficiency of 28.51% at a current density of 14.29 mA/cm^2. The present study further describes the modeling and performance of a low-concentration vanadium redox flow

battery. The experimental battery consistently performed as the COMSOL model predicted, though the experimental values tended to be exaggerated. Another flow battery with the same parameters will be developed in future and created to allow for the testing of a variety of electrolyte chemistries and electrolytes that include hydrogen peroxide.

Acknowledgment

The authors would like to express their sincere gratitude to Dr. Aicheng Chen from the Chemistry Department for his guidance and advice during the development of H-cell and Mike Speagle, lab technician of Sustainable Energy Lab, University of Guelph. This work is supported by the Natural Sciences and Engineering Research Council of Canada through the Engage Grant Program and Virox Technologies Inc., an industrial research partner.

Nomenclature

n = number of electrons transferred in the cell reaction, unitless
$\mathbf{v}$ = velocity vector of the electrolyte, m/s
A = electrodes active area, m^2
E = electrode potential, V
F = Faraday constant, C/mol
R = universal gas constant, J/mol K
T = temperature, K
i_l = electrolyte current density, A/m^2
i_{pos} = positive electrode current density, A/m^2
i_{neg} = negative electrode current density, A/m^2
k_d = dissociation reaction coefficient, unitless
r_d = dissociation source term, mol
z_i = valence charge for species i, unitless
C_i = concentration of species i in the electrolyte, mol/m^3
$E_{0,Pos}$ = standard reduction potential (positive electrode), V
$E_{0,Neg}$ = standard reduction potential (negative electrode), V
$E_{eq,pos}$ = equilibrium potential (positive terminal), V
$E_{eq,neg}$ = equilibrium potential (negative terminal), V
$\mathbf{N}_i$ = flux of the species i via diffusion, V m
c_c^e = species concentration in the electrolyte, mol/m^3
c_c^m = species concentration in the membrane, mol/m^3
C_V^e = bulk concentration of vanadium, mol/m^3
C_V^s = surface concentration of vanadium, mol/m^2
D_i^{eff} = effective diffusion coefficient for species i, m^2/s
α_i = chemical activity of species i, unitless
α_{pos} = charge transfer coefficient in the positive half-cell, dimensionless
α_{neg} = charge transfer coefficient in the negative half-cell, dimensionless
β = degree of dissociation, %
η_{pos} = positive half-cell overpotential, V
η_{neg} = negative half-cell overpotential, V
ϕ_s = electric potential of the solid phase of the electrode, V
ϕ_l = electrolyte potential, V
ρ_{fix} = fixed charge from the membrane
$\phi_{l,m}$ = potential shift at the electrolyte/membrane interface, V

Subscripts

c = species concentration
m = membrane

Superscripts

e = electrolyte
m = membrane

References

[1] Ibrahim, H., Ilinca, A., and Perron, J., 2008, "Energy Storage Systems—Characteristics and Comparisons," Renew. Sustain. Energy Rev., **12**(5), pp. 1221–1250.
[2] Miroshnikov, M., Kato, K., Babu, G., Thangavel, K. N., Mahankali, K., Hohenstein, E., Wang, H., Satapathy, S., Divya, K. P., Asare, H., Arava, L. M. R., Ajayan, P. M., and John, G., 2019, "Nature-Derived Sodium-Ion Battery: Mechanistic Insights Into Na-Ion Coordination Within Sustainable Molecular Cathode Materials," Am. Chem. Soc., **2**(12), pp. 8596–8604.
[3] Mahankali, K., Thangavel, K. N., Ding, Y., Putatunda, S. K., and Arava, L. M. R., 2019, "Interfacial Behavior of Water-in-Salt Electrolytes at Porous Electrodes and Its Effect on Supercapacitor Performance," Electrochim. Acta, **326**, p. 134989.
[4] Ponce de León, C., Frías-Ferrer, A., Gonzàlez-García, J., Szánto, D. A., and Walsh, F., 2006, "Redox Flow Cells for Energy Conversion," J. Power Sources, **160**(1), pp. 716–732.
[5] Wang, W., Luo, Q., Li, B., Wei, X., Li, L., and Yang, Z., 2013, "Recent Progress in Redox Flow Battery Research and Development," Adv. Funct. Mater., **23**(8), pp. 970–986.
[6] Ledjeff, K., and Reiner, A., 1988, "Iron/Chromium—Redox Battery: Battery Development for Photovoltaic Systems," Adv. Solar Energy Technol., **3**, pp. 2976–2979.
[7] Munaiah, Y., Suresh, S., Dheenadaylan, S., Pillai, V. K., and Ragupathy, P., 2014, "Comparative Electrocatalytic Performance of Single-Walled and Multiwalled Carbon Nanotubes for Zinc Bromine Redox Flow Batteries," J. Phys. Chem., **118**(27), pp. 14795–14804.
[8] Munaiah, Y., Dheenadaylan, S., Ragupathy, P., and Pillai, V. K., 2013, "High Performance Carbon Nanotube Based Electrodes for Zinc Bromine Redox Flow Batteries," ECS J. Solid State Sci. Technol., **2**(10), pp. M3182–M3186.
[9] Suresh, S., Ulaganathan, M., Venkatesan, N., Periasamy, P., and Ragupathy, P., 2018, "High Performance Zinc-Bromine Redox Flow Batteries: Role of Various Carbon Felts and Cell Configurations," J. Energy Storage, **20**, pp. 134–139.
[10] Rychcik, M., and Skyllas-Kazacos, M., 1988, "Characteristics of a New All-Vanadium Redox Flow Battery," J. Power Sources, **22**(1), pp. 59–67.
[11] Li, L., Kim, S., Wang, W., Vijayakumar, M., Nie, Z., Chen, B., Zhang, J., Xia, G., Hu, J., Graff, G., Liu, J., and Yang, Z., 2011, "A Stable Vanadium Redox-Flow Battery With High Energy Density for Large-Scale Energy Storage," Adv. Energy Mater., **1**(3), pp. 394–400.
[12] Parasuraman, A., Lim, T. M., Menictas, C., and Skyllas-Kazacos, M., 2012, "Review of Material Research and Development for Vanadium Redox Flow Battery Applications," Electrochim. Acta, **101**, pp. 27–40.
[13] Vafiadis, H., and Skyllas-Kazacos, M., 2006, "Evaluation of Membranes for the Novel Vanadium Bromine Redox Flow Cell," J. Membr. Sci., **279**(1–2), pp. 394–402.
[14] Gundlapalli, R., Kumar, S., and Sreenivas, J., 2018, "Stack Design Considerations for Vanadium Redox Flow Battery," INAE Lett., **3**(3), pp. 149–157.
[15] Li, X., Zhang, H., Mai, Z., Zhanga, H., and Vankelecom, I., 2011, "Ion Exchange Membranes for Vanadium Redox Flow Battery (VRB) Applications," Energy Environ. Sci., **4**(4), pp. 1147–1160.
[16] Castañeda, L. F., Walsh, F. C., Nava, J. L., and Ponce de León, C., 2017, "Graphite Felt as a Versatile Electrode Material: Properties, Reaction Environment, Performance and Applications," Electrochim. Acta, **258**, pp. 1115–1139.
[17] Aaron, D., Liu, Q., Tang, Z., Grim, G., Papandrew, A., Turhan, A., Zawodzinski, T., and Mench, M., 2012, "Dramatic Performance Gains in Vanadium Redox Flow Batteries Through Modified Cell Architecture," J. Power Sources, **206**, pp. 450–453.
[18] Zhou, X., Zhao, T., Zeng, Y., An, L., and Wei, L., 2016, "A Highly Permeable and Enhanced Surface Area Carbon-Cloth Electrode for Vanadium Redox Flow Batteries," J. Power Sources, **329**, pp. 247–254.
[19] Skyllas-Kazacos, M., 2003, "Novel Vanadium Chloride/Polyhalide Redox Flow Battery," J. Power Sources, **124**(1), pp. 299–302.
[20] Rahman, F., and Skyllas-Kazacos, M., 2009, "Vanadium Redox Battery: Positive Half-Cell Electrolyte Studies," J. Power Sources, **189**(2), pp. 1212–1219.
[21] Zhang, J., Li, L., Nie, Z., Chen, B., Vijayakumar, M., Kim, S., Wang, W., Schwenzer, B., Liu, J., and Yang, Z., 2011, "Effects of Additives on the Stability of Electrolytes for All-Vanadium Redox Flow Batteries," J. Appl. Electrochem., **41**(10), pp. 1215–1221.
[22] Wu, X., Liu, S., Wang, N., Peng, S., and He, Z., 2012, "Influence of Organic Additives on Electrochemical Properties of the Positive Electrolyte for All-Vanadium Redox Flow Battery," Electrochim. Acta, **78**, pp. 475–482.
[23] Chang, F., Hu, C., Liu, X., Liu, L., and Zhang, J., 2012, "Coulter Dispersant as Positive Electrolyte Additive for the Vanadium Redox Flow Battery," Electrochim. Acta, **60**, pp. 334–338.
[24] Wu, X., Liu, J., Xiang, X., Zhang, J., Hu, J., and Wu, Y., 2014, "Electrolytes for Vanadium Redox Flow Batteries," Pure Appl. Chem., **86**(5), pp. 661–669.
[25] Skyllas-Kazacos, M., Kazacos, G., Poon, G., and Verseema, H., 2010, "Recent Advances With the UNSW Vanadium-Based Redox Flow Batteries," Int. J. Energy Res., **34**(2), pp. 182–189.
[26] Park, S., Lee, H. J., Lee, H., and Kim, H., 2018, "Development of a Redox Flow Battery With Multiple Redox Couples at Both Positive and Negative Electrolytes for High Energy Density," J. Electrochem. Soc., **165**(14), pp. A3215–A3220.
[27] Menictas, C., and Skyllas-Kazacos, M., 2011, "Performance of Vanadium-Oxygen Redox Fuel Cell," J. Appl. Electrochem., **41**(10), pp. 1223–1232.
[28] An, L., Zhao, T., Zhou, X., Yan, X., and Jung, C., 2015, "A Low-Cost, High-Performance Zinc-Hydrogen Peroxide Fuel Cell," J. Power Sources, **275**, pp. 831–834.

[29] Xu, T., 2005, "Ion Exchange Membranes: State of Their Development and Perspective," J. Membr. Sci., **263**(1–2), pp. 1–29.
[30] Zhang, H., Zhang, H., Li, X., Mai, Z., and Zhang, J., 2011, "Nanofiltration (NF) Membranes: the Next Generation Separators for All Vanadium Redox Flow Batteries (VRBs)?," Energy Environ. Sci., **4**(5), pp. 1676–1679.
[31] Sun, B., and Skyllas-Kazacos, M., 1992, "Modification of Graphite Electrode Materials for Vanadium Redox Flow Battery Application—I. Thermal Treatment," Electrochim. Acta, **37**(7), pp. 1253–1260.
[32] Pezeshki, A. M., Clement, J. T., Veith, G. M., Zawodzinski, T. A., and Mench, M. M., 2015, "High Performance Electrodes in Vanadium Redox Flow Batteries Through Oxygen-Enriched Thermal Activation," J. Power Sources, **294**, pp. 333–338.
[33] Eifert, L., Banerjee, R., Jusys, Z., and Zeis, R., 2018, "Characterization of Carbon Felt Electrodes for Vanadium Redox Flow Batteries: Impact of Treatment Methods," J. Electrochem. Soc., **165**(11), pp. A2577–A2586.
[34] González, Z., Sánchez, A., Blanco, C., Granda, M., Menéndez, R., and Santamaría, R., 2011, "Enhanced Performance of a Bi-Modified Graphite Felt as the Positive Electrode of a Vanadium Redox Flow Battery," Electrochem. Commun., **13**(12), pp. 1379–1382.
[35] Wei, L., Zhao, T., Zhao, G., An, L., and Zeng, L., 2016, "A High-Performance Carbon Nanoparticle-Decorated Graphite Felt Electrode for Vanadium Redox Flow Batteries," Appl. Energy, **176**, pp. 74–79.
[36] Yun, N., Park, J. J., Park, O., Lee, K. B., and Yang, J. H., 2018, "Electrocatalytic Effect of NiO Nanoparticles Evenly Distributed on Agraphite Felt Electrode for Vanadium Redox Flow Batteries," Electrochim. Acta, **278**, pp. 226–235.
[37] Flox, C., Skoumal, M., Rubio-Garcia, J., Andreu, T., and Morante, J. R., 2013, "Strategies for Enhancing Electrochemical Activity of Carbon-Based Electrodes for All-Vanadium Redox Flow Batteries," Appl. Energy, **109**, pp. 344–351.
[38] Kim, K. J., Kim, Y.-J., Kim, J.-H., and Park, M.-S., 2011, "The Effects of Surface Modification on Carbon Felt Electrodes for Use in Vanadium Redox Flow Batteries," Mater. Chem. Phys., **131**(1–2), pp. 547–553.
[39] Bhattarai, A., Wai, N., Schweiss, R., Whitehead, A., Lim, T. M., and Hng, H. H., 2017, "Advanced Porous Electrodes With Flow Channels for Vanadium Redox Flow Battery," J. Power Sources, **341**, pp. 83–90.
[40] Li, W., Liu, J., and Yan, C., 2011, "Graphite–Graphite Oxide Composite Electrode for Vanadium Redox Flow Battery," Electrochim. Acta, **56**(14), pp. 5290–5294.
[41] He, Z., Li, M., Li, Y., Zhu, J., Jiang, Y., Meng, W., Zhou, H., Wang, L., and Dai, L., 2018, "Flexible Electrospun Carbon Nanofiber Embedded With TiO_2 as Excellent Negative Electrode for Vanadium Redox Flow Battery," Electrochim. Acta, **281**, pp. 601–610.
[42] Li, W., Liu, J., and Yan, C., 2011, "Multi-Walled Carbon Nanotubes Used as an Electrode Reaction Catalyst for VO2+/VO2+ for a Vanadium Redox Flow Battery," Carbon, **49**(11), pp. 3463–3470.
[43] Wang, Q., Qu, Z., Jiang, Z., and Yang, W., 2018, "Numerical Study on Vanadium Redox Flow Battery Performance With Non-Uniformly Compressed Electrode and Serpentine Flow Field," Appl. Energy, **220**, pp. 106–116.
[44] Gurieff, N., Timchenko, V., and Menictas, C., 2018, "Variable Porous Electrode Compression for Redox Flow Battery Systems," Batteries, **4**(4), pp. 1–10.
[45] Darling, R. M., and Perry, M. L., 2014, "The Influence of Electrode and Channel Configurations on Flow Battery Performance," J. Electrochem. Soc., **161**(9), pp. A1381–A1387.
[46] Knudsen, E., Albertus, P., Cho, K., Weber, A., and Kojic, A., 2015, "Flow Simulation and Analysis of High-Power Flow Batteries," J. Power Sources, **299**, pp. 617–628.
[47] Xu, Q., Zhao, T., and Leung, P., 2013, "Numerical Investigations of Flow Field Designs for Vanadium Redox Flow Batteries," Appl. Energy, **105**, pp. 47–56.
[48] Houser, J., Clement, J., Pezeshki, A., and Mench, M. M., 2016, "Influence of Architecture and Material Properties on Vanadium Redox Flow Battery Performance," J. Power Sources, **302**, pp. 369–377.
[49] Messaggi, M., Mereu, R., Baricci, A., Inzoli, F., Casalegno, A., and Zago, M., 2018, "Analysis of Flow Field Design on Vanadium Redox Flow Battery Performance: Development of 3D Computational Fluid Dynamic Model and Experimental Validation," Appl. Energy, **228**, pp. 1057–1070.
[50] Tang, A., Bao, J., and Skyllas-Kazacos, M., 2014, "Studies on Pressure Losses and Flow Rate Optimization in Vanadium Redox Flow Battery," J. Power Sources, **248**, pp. 154–162.
[51] Lee, N. J., Lee, S.-W., Kim, K. J., Kim, J.-H., Park, M.-S., Jeong, G., Kim, Y.-J., and Byun, D., 2012, "Development of Carbon Composite Bipolar Plates for Vanadium Redox Flow Batteries," Bull. Korean Chem. Soc., **33**(11), pp. 3589–3592.
[52] Park, M., Jung, Y.-J., Ryu, J., and Cho, J., 2014, "Material Selection and Optimization for Highly Stable Composite Bipolar Plates in Vanadium Redox Flow Batteries," J. Mater. Chem. A, **2**(38), pp. 15808–15815.
[53] Han, J., Yoo, H., Kim, M., Lee, G., and Choi, J., 2017, "High-Performane Bipolar Plate of Thin IrOx-Coated TiO_2 Nanotubes in Vanadium Redox Flow Batteries," Catal. Today, **295**, pp. 132–139.
[54] Ma, X., Zhang, H., Sun, C., Zou, Y., and Zhang, T., 2012, "An Optimal Strategy of Electrolyte Flow Rate for Vanadium Redox Flow Battery," J. Power Sources, **203**, pp. 153–158.
[55] Cunha, Á, Martins, J., Rodrigues, N., and Brito, F. P., 2014, "Vanadium Redox Flow Batteries: A Technology Review," Int. J. Energy Res., **39**(7), pp. 889–918.
[56] Skyllas-Kazacos, M., Cao, L., Kazacos, M., Kausar, N., and Mousa, A., 2016, "Vanadium Electrolyte Studeis for the Vanadium Redox Battery—A Review," ChemSusChem Rev., **9**(13), pp. 1521–1543.
[57] Chanyong, C., Kim, S., Kim, R., Choi, Y., Kim, S., Jung, H. Y., Yang, J. H., and Kim, H. T., 2017, "A Review of Vanadium Electrolytes for Vanadium Redox Flow Batteries," Renew. Sustain. Energy Rev., **69**, pp. 263–274.
[58] Knehr, K. W., Agar, E., Dennison, C. R., Kalidindi, A. R., and Kumbur, E. C., 2012, "A Transient Vanadium Flow Battery Model Incorporating Vanadium Crossover and Water Transport Through the Membrane," J. Electrochem. Soc., **159**(9), pp. A1446–A1459.
[59] Knehr, K., and Kumbur, E., 2011, "Open Circuit Voltage of Vanadium Redox Flow Batteries: Discrepancy Between Models and Experiments," Electrochem. Commun., **13**(4), pp. 342–345.
[60] Shah, A., Watt-Smith, M., and Walsh, F., 2008, "A Dynamic Performance Model for Redox-Flow Batteries Involving Soluble Species," Electrochim. Acta, **53**(27), pp. 8087–8100.